ESA Climate Change Initiative

aerosol_cci

ALGORITHM THEORETICAL BASIS DOCUMENT (ATBD)

MSG/SEVIRI

THE CISAR ALGORITHM

Prepared by : Y. Govaerts, M. Luffarelli, C. Goossens and A. Damman (Rayference)

Reference : CISAR-ATBD-V1.0

Version : V1.0

Date : January 2017

rayference

Document Change Record

Doc. Version	Date	CISAR Release	Remarks
Version 0.2	June 2016	-	First released version
Version 1.0	January 2017	00.00	

Table of Contents

List of Acronyms

AOT	Aerosol Optical Thickness
ATBD	Algorithm Theoretical Basis Document
AU	Astronomical Unit
BRF	Bidirectional Reflectance Factor
CISAR	Combined Inversion of Surface and AeRosol
DHR	Directional Hemispherical Reflectance
EQMPN	Equivalent Model Parameter Noise
ESA	European Space Agency
GEDAP	GEneric DAta Processing Chain
IFOV	Instantaneous Field Of View
LUT	Look-Up Table
MISR	Multiangle Imaging Spectro-Radiometer
MSG	Meteosat Second Generation
OE	Optimal Estimation
RPV	Rahman - Pinty - Verstraete BRF model
RTM	Radiation Transfer Model
SAF	Satellite Application Facility
SEVIRI	Spinning Enhanced Visible and InfraRed Imager
TOA	Top Of Atmosphere

List of To Be Defined

EXECUTIVE SUMMARY

This document describes the algorithm used to generate an hourly aerosol optical thickness product from SEVIRI observations. As the algorithm derives the total column aerosol optical thickness, it does not discriminate between tropospheric and stratospheric aerosols. This algorithm relies on a joint retrieval of surface reflectance and aerosol optical thickness based on the inversion of a coupled surface-atmosphere radiative transfer model.

The forward model is explicitly solved during the inversion process, *i.e.*, it does not rely on pre-computed solutions, allowing a continuous variation of the state variables in the solution space.

The retrieval scheme is based on an Optimal Estimation (OE) approach where the cost function accounts for the differences between the observations and the forward radiative transfer model, the retrieved state variables and their prior information and finally smoothness constraints on temporal and spectral variations of the aerosol properties.

1 INTRODUCTION

This ATBD describes the CISAR algorithm that infers hourly fine and coarse mode aerosol optical thicknesses over land and sea surfaces from observations acquired by the SEVIRI radiometer in bands 0.6, 0.8 and 1.6μm. As the algorithm derives the total column aerosol optical thickness, it does not discriminate between tropospheric and stratospheric aerosols. This algorithm relies on a joint retrieval of surface reflectance and aerosol optical thickness based on the inversion of a coupled surface-atmosphere radiative transfer model.

The forward model is explicitly solved during the inversion process, *i.e.*, it does not rely on pre-computed solutions, allowing a continuous variation of the state variables in the solution space.

The retrieval scheme is based on an Optimal Estimation (OE) approach where the cost function accounts for the differences between the observations and the forward radiative transfer model, the retrieved state variables and their prior information and finally smoothness constraints on temporal and spectral variations of the aerosol properties.

The proposed algorithm capitalizes on the capability of SEVIRI to acquire data every 15 minutes to perform an angular sampling of the same radiance field under various solar geometries. The temporal accumulation of data acquired under different illumination conditions is thus used to form a virtual multi-angular measurement system. SEVIRI data are thus accumulated in the 0.6, 0.8 and 1.6μm bands during a given period to form the measurement vector. The primary objective of this accumulation is to document the surface BRF. It is therefore performed during N_d days to minimize the effects of clouds and maximize the angular sampling of the surface BRF. During this accumulation period, surface properties are assumed temporally invariant. The inversion procedure takes place at the end of this accumulation period to retrieve the surface reflectance in each band and the hourly Aerosol Optical Thickness (AOT) at 0.55μm.

2 INSTRUMENT CHARACTERISTICS

The primary objective of Meteosat Second Generation (MSG) mission is the continuous observation in near real-time of the Earth's full disk. The Spinning Enhanced Visible and Infrared Imager (SEVIRI) imaging radiometer is fulfilling this objective in 12-channel observing the Earth–atmosphere system. Eleven channels observe the Earth's full disk with a 15 min repeat cycle from 0.6 to 13μm. Among these 11 channels, three are located in the solar spectrum and are centred around 0.64μm, 0.81μm and 1.64μm. A high-resolution visible (HRVIS) channel covers half of the full disk in the east–west direction and the full disk in the North–South direction. This channels ranges from 0.4 to 1.1μm. Radiances are quantized on 10 bits.

MSG nominal position is 0° over the equator in a geostationary orbit. The sampling distance between two adjacent pixels at the sub-satellite point is 3km for the visible bands and 1km for the HRVIS band. The high-resolution visible channel has a spatial resolution of 1.67 km, as the oversampling factor is 1.67 the sampling distance. The corresponding values for the eight thermal IR and the other three solar channels are 4.8km spatial resolution, with an oversampling factor of 1.6 that corresponds to a sampling distance of 3 km for nadir view. The instantaneous field of view (IFOV) corresponds to the area of sensitivity for each picture element. Since the aperture angle for each IFOV is constant, it follows that the corresponding area at the surface varies with satellite-viewing angle. The telescope optical layout is based on a three-mirror concept with a primary mirror of 51 cm in diameter. The optical bench of the solar channels is at a temperature of 293 K.

The imaging is performed, by combining satellite spin and rotation (stepping) of the scan mirror. The images are taken from South to North and East to West (Aminou et al. 1997). The E–W scan is achieved through the rotation of the satellite with a nominal spin rate of 100 revolutions min^{-1}. The spin axis is nominally parallel to the North–South axis of the Earth. The scan from South to North is achieved through a scan mirror covering the Earth's disk with about 1250 scan lines; this provides 3750 image lines for channels 1–11 since three detectors for each channel are used for the imaging. For the HRVIS (channel 12) nine detectors sweep the Earth for one line scan. A complete image, that is, the full disk of the Earth, consists of nominally 3712 × 3712 pixels for channels 1–11. The HRVIS channel covers only half the full disk in the E–W direction and therefore a complete image consists of 11 136 × 5568 pixels.

A nominal repeat cycle is a full-disk imaging of about 12 min, followed by the calibration of thermal IR channels with an on-board blackbody that is inserted into the optical path of the instrument. Then the scan mirror returns to its initial scanning position. There is no on-board device for the calibration of the solar channels. It relies on a operational vicarious method running operational at EUMETSAT (Govaerts 2004; Govaerts et al. 2004).

3 FORWARD MODEL

3.1 Vertical structure

The forward model $y_m(\mathbf{x}, \mathbf{b}; \mathbf{m})$ simulates the TOA Bidirectional Reflectance Factor as a function of the viewing and illumination angles, the spectral band $\tilde{\lambda}$, the state of the atmosphere and underlying surface. This model depends on the retrieved state variables $\mathbf{x}$, the model parameters $\mathbf{b}$ and finally the observation conditions. The independent parameters, such as the acquisition geometry or the spectral band, that determine these observation conditions are denoted $\mathbf{m}$. The radiative transfer equation is solved with the Matrix Operator Method (Fischer and Grassl 1984) optimised by Liu and Ruprecht (1996) for a finite number of quadrature points.

The model is designed to simulate radiometer observations acquired with a spectral interval characterized by the spectral response of the processed radiometer. The gaseous transmittance in these intervals is precomputed and stored in look-up tables. All other operations are performed online, *i.e.*, during the inversion process. The model separates the single scattering contribution from the multiple scattering contribution. The multiple scattering contribution is solved in the Fourier space.

The forward model relies on the same atmospheric vertical structure as in Govaerts et al. (2010), *i.e.*, a three-level system containing two layers that are radiatively coupled (Figure 1). The hight of level Z_a is determined from an aerosol hight climatology derived from level 3 aerosol profile product obtained with the CALIOP (Cloud- Aerosol LIdar with Orthogonal Polarization) instrument on-board CALIPSO might be considered. The aerosol profile product reports monthly mean profiles of aerosol optical properties on a uniform global spatial grid. The spatial resolution is 5° in longitude, 2° in latitude and 60 m along vertical. This is a tropospheric product that reports averaged values at altitudes below 12km. The lower level z_0 is the surface. Over land surface reflectance is represented by the so-called RPV model which has four parameters (ρ_0, k, Θ, h) that are all wavelength dependent (Rahman et al. 1993). Over sea surface, BRF is simulated with the Cox-Munk model as implemented in Vermote et al. (1997). The lower layer L_a, ranging from level z_0 to z_a contains the aerosol particles. Molecular scattering and absorption are also taking place in that layer. The upper layer L_g, ranging from z_a to z_s is only subject to molecular absorption. The uncertainty of this model is estimated on Section 4.2.2.3.

3.2 General mathematical formulation

The forward model expresses the TOA BRF in a given spectral band $\tilde{\lambda}$ as a sum of the single and multiple scattering contributions which formally writes

$$y_m(\mathbf{x}, \mathbf{b}; \mathbf{m}) \;=\; T_{L_g}(\mathbf{b}; \mathbf{m}) \, \frac{I_s^{\uparrow}(\mathbf{x}, \mathbf{b}; \mathbf{m}) \;+\; I_m^{\uparrow}(\mathbf{x}, \mathbf{b}; \mathbf{m})}{E_0^{\downarrow}(\mathbf{m})\mu_0} \tag{1}$$

where

$I_s^{\uparrow}(\mathbf{x}, \mathbf{b}; \mathbf{m})$ is the upward radiance field at level z_a due to the single scattering;

$I_m^{\uparrow}(\mathbf{x}, \mathbf{b}; \mathbf{m})$ is the upward radiance field at level z_a due to the multiple scattering;

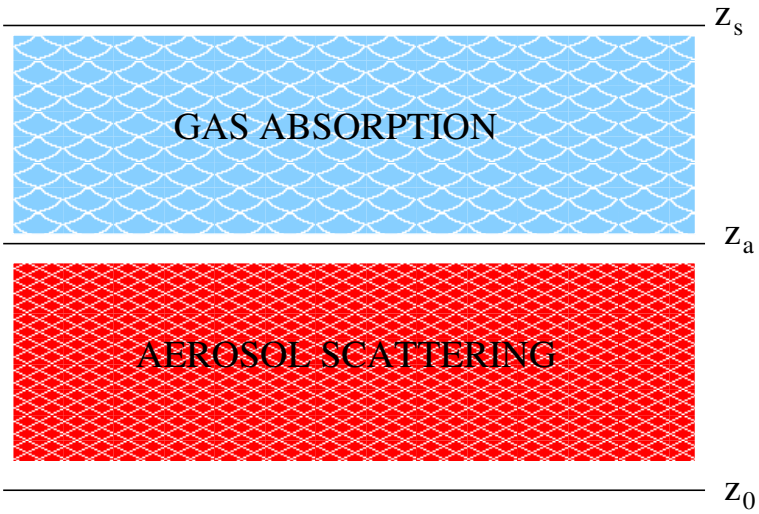

Figure 1: CISAR forward model vertical structure.

$T_{L_g}(\mathbf{b};\mathbf{m})$ denotes the total transmission factor in the T_{L_g} layer;

$E_0^{\downarrow}(\mathbf{m})$ denotes the solar irradiance at level z_s corrected for the Sun-Earth distance variations.

μ_0 is the cosine of the sun zenith angle. The single scattering contribution writes

$$I_s^{\uparrow}(\mathbf{x},\mathbf{b};\mathbf{m}) = \frac{E_0^{\downarrow}(\mathbf{m})\ \mu_0}{\pi} \exp\left(\frac{-\tau_{L_a}}{\mu_0}\right)\ r_s(\mathbf{x},\mathbf{b};\mathbf{m})\ \exp\left(\frac{-\tau_{L_a}}{\mu_v}\right) \tag{2}$$

where $E_0^{\downarrow}$ is the TOA solar irradiance in direction μ_0 corrected for the Sun-Earth distance, τ_{L_a} total optical thickness of layer L_a. μ_0 and μ_v are the cosine of the illumination and viewing zenith angles respectively. $r_s(\mathbf{x},\mathbf{b};\mathbf{m})$ is the surface reflectance corresponding to the illumination and viewing geometries.

The multiple scattering contribution $I_m^{\uparrow}(\mathbf{x},\mathbf{b};\mathbf{m})$ is solved in the Fourier space for all illumination and viewing directions of the quadrature directions N_θ for $2N_\theta - 1$ azimuthal directions with the method proposed by (Liu and Ruprecht 1996). The contribution $I_m^{\uparrow}(\mathbf{x},\mathbf{b};\mathbf{m})$ in the direction (Ω_0,Ω_v) is interpolated from the surrounding quadrature directions.

3.3 Surface properties

3.3.1 Land surface

The surface reflectance is represented by the RPV model (Rahman et al. 1993) which has four parameters $\mathbf{x}_s = (\rho_0, k, \Theta, h)$ that are all wavelength dependent. The individual contribution of these four parameters to the total surface BRF is illustrated on Figure (2). Specifically,

- ρ_0 controls the mean amplitude of the BRF. This parameter strongly varies with the wavelength and mainly controls the mean surface reflectance. It varies between 0 and 1.

k determines the bowl shape of the BRF. It varies between 0 and 2.

Θ is the asymmetry parameter of the Henyey-Greenstein phase function and also varies between -1 and 1.

h controls the amplitude of the hot-spot, *i.e.*, the "porosity" of the medium. This parameter takes only positive values and typically varies between 0 and 1.

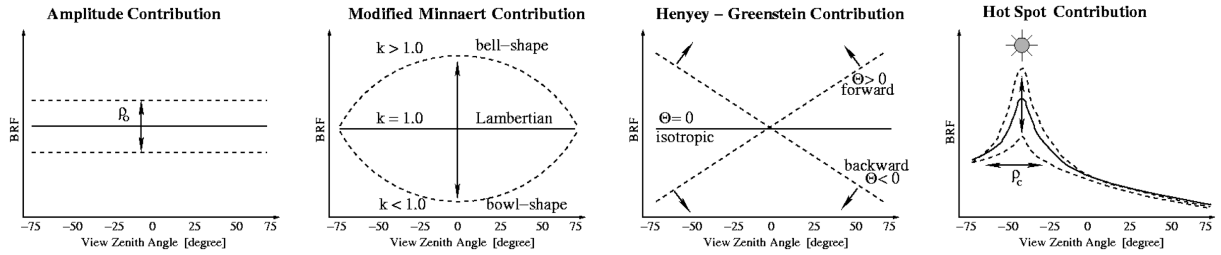

Figure 2: Contribution of the four RPV parameters to the total surface BRF.

Engelsen et al. (1996) analysed in detail on the performance and limits of applicability of this parametric model. The RPV model formally writes

$$r_s(\mathbf{x},\mathbf{b};\mathbf{m}) = \rho_0(\tilde{\lambda})\,\breve{\rho}_s(k(\tilde{\lambda}),\Theta(\tilde{\lambda}),h(\tilde{\lambda});\mu_0,-\mu_v,\phi_r) \tag{3}$$

where ρ_0 and $\breve{\rho}_s(k(\tilde{\lambda}),\Theta(\tilde{\lambda}),h(\tilde{\lambda});-\mu_v,\mu_0,\phi_r)$ describe the amplitude and the angular field of the surface BRF, respectively. This latter quantity is expressed by:

$$\breve{\rho}_s(k(\tilde{\lambda}),\Theta(\tilde{\lambda}),h(\tilde{\lambda});\mu_0,-\mu_v,\phi_r) = M_I(\mu_0,-\mu;k(\tilde{\lambda}))\,F(g;\Theta(\tilde{\lambda}))\,H(h(\tilde{\lambda});G) \tag{4}$$

where:

$$M_I(\mu_0,-\mu;k(\tilde{\lambda})) = \frac{\mu_0^{k-1}\mu^{k-1}}{(\mu_0+\mu_v)^{1-k}} \tag{5}$$

$$F(g;\Theta(\tilde{\lambda})) = \frac{1-\Theta^2(\tilde{\lambda})}{[1+2\Theta(\tilde{\lambda})\cos g+\Theta^2(\tilde{\lambda})]^{3/2}} \tag{6}$$

$$H(h(\tilde{\lambda});G) = 1+\frac{1-h(\tilde{\lambda})}{1+G} \tag{7}$$

$$\cos g = \cos\theta\cos\theta_0+\sin\theta\sin\theta_0\cos\phi_r \tag{8}$$

$$G = [\tan^2\theta_0+\tan^2\theta-2\tan\theta_0\tan\theta\cos\phi_r]^{1/2} \tag{9}$$

The relative azimuth angle, ϕ_r, is zero when the source of illumination is behind the satellite.

3.3.2 Sea surface

The total reflectance over sea surfaces is defined as being composed of three terms, representing three different sources of upwelling radiance fields. Firstly, light can be reflected off white caps in the rough ocean surface; secondly, it can be reflected off the sea surface itself. The relative contributions from

these two factors will depend on the roughness of the sea surface, which is dependent on the surface wind speed v_{z_0}. Thirdly, light penetrating the surface can be scattered back up into the atmosphere by molecules within the water, such as water and dissolved pigments. Considering the combination of these terms, the sea surface reflectance in spectral band $\tilde{\lambda}$ writes

$$r_s(\mathbf{x}, \mathbf{b}; \mathbf{m}) = \rho_{wc}(v_{z_0}; \tilde{\lambda}) + (1 - W)\rho_{gl}(v_{z_0}; \tilde{\lambda}) + (1 - \rho_{gl}(v_{z_0}; \tilde{\lambda}))\rho_{sw} \tag{10}$$

where

ρ_{wc} is the reflectance due to white caps

ρ_{gl} is the specular reflectance at the ocean surface

ρ_{sw} is the scattered reflectance emerging from sea water

W is the relative area covered with white caps

v_{z_0} is the surface wind speed.

The reflectance of the white cap is taken from Koepke (1984) and the specular contribution from Cox and Munk (1954). For the scattered reflectance emerging from sea water, a constant chlorophyll concentration of 0.1 [mg/m^3] is assumed (Morel 1988).

3.4 Scattering layer properties

The layer L_a contains a set of aerosol classes characterized by their single scattering properties, *i.e.*, the single scattering albedo $\omega_0(\tilde{\lambda})$ and phase function $P(\tilde{\lambda})$. These different aerosols classes representing the fine and coarse modes are mixed into this layer according to their respective optical thickness τ_c with the total aerosol optical thickness τ_a of the layer being equal to $\tau_a = \sum_i \tau_c(i)$.

The number of Legendre coefficients N_κ used to define the phase function of the various aerosol classes is equal to $2N_\theta - 1$. When the last Legendre moment $N_\kappa - 1$ (equal to the coefficient N_κ) is not equal to zero, the delta-M approximation is applied (Wiscombe 1977). The forward peak of the delta-M approximation $\alpha_d(\tilde{\lambda})$ is equal to the coefficient $P(N_\kappa)$. To better capture the strong forward peak of the phase function, it is represented as a linear combination of a Dirac's delta function representing a certain amount α_d of forward scattering and a modified phase function p' with reduced probability of forward scattering for angles smaller than a certain threshold value. The Legendre coefficients κ_j, after application of the delta-M approximation, become

$$c_j = \frac{\kappa_j - \alpha_d}{1 - \alpha_d} \, . \tag{11}$$

The corrected optical thickness and single scattering albedo of the corresponding aerosol class become

$$\tau_c'(\tilde{\lambda}) = (1 - \omega_0(\tilde{\lambda})\alpha_d)\, \tau_c(\tilde{\lambda}) \tag{12}$$

$$\omega_0'(\tilde{\lambda}) = \frac{1 - \alpha_d}{1 - \omega_0(\tilde{\lambda})\alpha_d}\, \omega_0(\tilde{\lambda}) \tag{13}$$

The choice of N_θ and thereby N_κ is critical. Large values of N_θ provides accurate simulations which translates into important additional computer time. Conversely, too small values lead to an important truncation of the forward peak as is the case for large aerosol particles. A good trade-off is to set $N_\theta = 10$ though a value of 6 would still provide acceptable solutions in case computer time becomes critical.

The layer total optical thickness $\tau_{L_a}(\tilde{\lambda})$ in the spectral band $\tilde{\lambda}$ is expressed as the sum of the gaseous optical depth $\tau_g(\tilde{\lambda})$ and extinction optical depths $\tau_a(\tilde{\lambda})$ and $\tau_m(\tilde{\lambda})$ resulting from the particle and molecular (Rayleigh) scattering

$$\tau_{L_a}(\tilde{\lambda}) = \tau_g(\tilde{\lambda}) + \tau_a(\tilde{\lambda}) + \tau_m(\tilde{\lambda}) \tag{14}$$

The molecular scattering optical thickness τ_m is based on the refraction index of the air calculated with Edlen's formulae. For each processed spectral band $\tilde{\lambda}$, the water vapour, ozone and well-mixed gases of fixed concentration composed oxygen (O_2), carbon dioxide (CO_2), methane (CH_4), nitrous oxide (N_2O) and carbon monoxide (CO)) transmittance is pre-computed and stored in LUT. For the first two gases, total column concentration should be provided. The concentration of the other gases are fixed according to a US76 vertical profile. This vertical profile is used to partition their respective concentration in layers L_a and L_g as described in Section 3.1.

3.5 Gaseous layer properties

It is assumed that only molecular absorption is taking place in the gaseous layer. The height of level z_a is used to partition the TCWV and TCO3 concentration in each layer assuming a US76 standard atmosphere vertical profile. T_{L_g} denotes the total transmission of that layer.

3.6 Forward model gradients

The derivatives $\mathbf{K}_x$ (Jacobian matrix) with respect to the forward model $y_m(\mathbf{x}, \mathbf{b}; \mathbf{m})$ are calculated as forward finite differences.

3.7 State vector

The state vector $\mathbf{x}$ is composed of the parameters $\mathbf{x}_s$ defining the surface reflectance $r_s(\mathbf{x}, \mathbf{b}; \mathbf{m})$ in the three SEVIRI bands and the aerosol fine and coarse mode optical thickness $\mathbf{x}_a = \{\tau_f, \tau_c\}$. The state parameters defining the radiative properties of the observed medium are divided into two categories. The first one, noted $\mathbf{x}$, represents the state variables that are retrieved from the observations $\mathbf{y}_{\Omega\tilde{\Lambda}}$ and is referred to as the *state vector*. The second one, noted $\mathbf{b}$, represents those parameters that also have a non-negligeable radiative effects on the observed medium but may not be reliably estimated from those measurements. They are referred to as the *model parameters* and are obtained from external source of information. The size of the state vector is noted n_x.

The model parameters are composed of the ozone, water vapour total column content, surface pressure, wind speed and direction, and aerosol layer height.

$$\mathbf{b} = \left\{U_{O_3}, U_{H_2O}, P_{z_0}, v_{z_0}, v_\phi, h_a\right\}. \tag{15}$$

Surface pressure, water vapour, ozone total column content and surface wind speed are taken from European Centre for Mid-Range Weather Forecasts (ECMWF) data. The aerosol layer height h_a is set to 2km. The surface wind speed is used only over water.

4 ALGORITHM DESCRIPTION

4.1 Outline

The CISAR algorithm is composed of the following major steps:

1. **Pre-processing**
   A series of pre-processing operations are performed prior to the inversion. The primary purpose of this pre-processing is the accumulation of SEVIRI data during a given period to form a multi-spectral and multi-angular observation vector. It also collects ancillary information required for the inversion and perform some additional computations such as observation uncertainty estimation and prior information definition. These pre-processing steps are:

   (a) Input data accumulation (Section 4.2)
   In this step, all information needed to perform the inversion is collected and accumulated. It concerns essentially the preparation of the measurement vector. For each pixel, SEVIRI radiances are accumulated during several days together with requested ancillary information such as the cloud mask, the total gaseous amount, the geometry, band irradiance and finally all relevant information for the computation of the radiometric uncertainties.

   (b) *a priori* information definition (Section 4.2.1)
   The *a priori* information is prepared from the best retrieval selected in the temporal compositing of the previous application cycle or default values when the processing of a time series is initiated.

   (c) Measurement noise estimation (Section 4.2.2)
   The radiometric noise of the observation vector is estimated.

2. **Angular and Spectral Inversion**
   The angular and spectral inversion for the retrieval of the aerosol and surface reflectance properties is performed individually for every processed pixel.

   (a) Cloud filtering (Section 4.3.1)
   A cloud mask is applied on the observation vector to remove all the cloud observations.
   Additionally, during this processing, only one clear-sky SEVIRI observation per hour is kept.

   (b) Inversion (Section 4.3.2.1)
   The state vector is estimated from the measurement vector. The forward model is estimated at each inversion step.

   (c) Retrieval uncertainty estimation (Section 4.3.4)
   The uncertainty of the solution is estimated.

   (d) Quality control (Section 4.3.3)
   TBD

3. **Product generation** (Section 4.4)
   The CISAR algorithm delivers the aerosol hourly optical thickness in each process spectral band and an extrapolation of the optical thickness at 0.55μm.

4.2 Pre-processing

This module collects all the information needed to perform the inversion. These data are listed in Section (6).

The observation information consists of all available daylight clear-sky slots acquired under different illumination conditions in the 0.6, 0.8 and 1.6μm SEVIRI bands. These observations are accumulated during a period of N_d days to form a multi-angular observation vector. SEVIRI acquires radiances $R(\Omega_0, \Omega_v, \tilde{\lambda}, z_s, \mathbf{p})$ with the geometry $\Omega = (\Omega_0, \Omega_v)$ in a spectral interval $\tilde{\lambda}$ when the radiometer is viewing a pixel $\mathbf{p}$ on the Earth from the level z_s. Only observations acquired with sun and viewing zenith angles smaller than $\theta_{\max}$ are considered.

For the purpose of the retrieval process, these radiances are converted into BRF with

$$\mathbf{y}(\Omega_0, \Omega_v, \tilde{\lambda}, \mathbf{p}) = \mathbf{y}(t, \tilde{\lambda}, \mathbf{p}) = \frac{\pi\, R(\Omega_0, \Omega_v, \tilde{\lambda}, z_s, \mathbf{p})\, d_{\odot}^2(t)}{E_0(\tilde{\lambda}, z_s)\, \mu_0} \tag{16}$$

where $d_{\odot}$ is the Sun-Earth distance at time t in Astronomical Unit (AU) and $E_0(\tilde{\lambda})$ is exo-atmospheric solar irradiance in the SEVIRI channel $\tilde{\lambda}$. $\{\Omega_0, \Omega_v, \tilde{\lambda}, z_s, \mathbf{p}\}$ constitute the independent parameters determining the observation conditions and are denoted $\mathbf{m} = \{\Omega_0, \Omega_v, \tilde{\lambda}, z_s, \mathbf{p}\}$.

For a given band, all observations sequentially accumulated during N_d days to form a virtual multi-angular observation system. The corresponding measurement vector is noted

$$\mathbf{y}_{\Omega}(\tilde{\lambda}, z_s, \mathbf{p}) = \mathbf{y}_m(\Omega_0(t_1), \cdots, \Omega_0(t_N), \Omega_v, \tilde{\lambda}, z_s, \mathbf{p}) = \mathbf{y}_m(t_1, \cdots, t_N, \Omega_v, \tilde{\lambda}, z_s, \mathbf{p}) = \mathbf{y}_{\Omega\tilde{\lambda}}(\Omega_v, z_s, \mathbf{p}). \tag{17}$$

When all spectral bands are considered, the measurement vector is noted in one of the following two way

$$\mathbf{y}_{\Omega\tilde{\Lambda}} = \{\mathbf{y}_{\Omega}(\tilde{\lambda}_1), \mathbf{y}_{\Omega}(\tilde{\lambda}_2), \mathbf{y}_{\Omega}(\tilde{\lambda}_3)\} \tag{18}$$

$$\mathbf{y}_{T\tilde{\Lambda}} = \{\mathbf{y}_{T}(\tilde{\lambda}_1), \mathbf{y}_{T}(\tilde{\lambda}_2), \mathbf{y}_{T}(\tilde{\lambda}_3)\} \tag{19}$$

4.2.1 Prior information

4.2.1.1 Prior information on the surface parameter magnitude The prior information $\mathbf{x}_b$ on the state of the surface $\mathbf{x}_s$ is defined from the analysis of the solutions $\hat{\mathbf{x}}(d)$ retrieved during the processing of the previous accumulation period. When CISAR runs for the first time, the prior information $\mathbf{x}_b$ of $\mathbf{x}_s$ is a default or climatological values with a corresponding very large uncertainties σ_{x_b}.

After the processing of the first accumulation period, prior information $\mathbf{x}_b$ is updated with the *a posteriori* solution. Specifically, the running mean and range in which the parameters vary are estimated based on the previous solutions during a certain time window N_r days long. Hence, the at prior information $\mathbf{x}_b$ time t_d the estimation of the prior information $\mathbf{x}_b(t_d)$ and associated uncertainty $\sigma_{x_b}(t_d)$ write

$$\mathbf{x}_b(t_d) = \frac{\sum_{t_i=0}^{t_d-1} \hat{\mathbf{x}}(t_i)}{N_r} \quad (20)$$

$$\sigma_{x_b}(t_d) = \frac{\max_{t_i \in N_r} \hat{\mathbf{x}}(t_i) - \min_{t_i \in N_r} \hat{\mathbf{x}}(t_i)}{2} \quad (21)$$

When not enough solutions $\hat{\mathbf{x}}(t_i)$ are available in the interval N_r, the prior information of the accumulation period t_d and its associated uncertainty are taken from the results of the previous accumulation period index $t_d - 1$. Such situation will typically occur at the beginning of a processing. If the processing of the last period $t_d - 1$ is successful, the surface prior value at t_d is updated to

$$\mathbf{x}_b(t_d) = \hat{\mathbf{x}}(t_d - 1) \quad (22)$$

$$\sigma_{x_b}(t_d) = \max(\sigma_{\hat{\mathbf{x}}}(t_d - 1), \sigma_{\min}) \quad (23)$$

where $\sigma_{\min}$ is the smallest allowed uncertainty on the surface prior values. Additionally, the update of $\mathbf{x}_b(t_d)$ is constrained by the following conditions

$$\left(\frac{\mathbf{x}_b(t_d)}{t_d}\right)^2 < (\sigma_{\min})^2 \quad (24)$$

When the processing of the previous period is not successful, *e.g.*, there were too few observations, the prior is kept with the same value, *i.e.*, $\mathbf{x}_b(t_d) = \mathbf{x}_b(t_d - 1)$ and the associated uncertainty is set to

$$\sigma_{x_b}(t_d) = \sigma_{x_b}(t_d - 1)\ 1.05^{N_d} \quad (25)$$

such that if this situation lasts several accumulation periods, the uncertainty of $\mathbf{x}_b$ will become larger and larger. The values σ_{x_b} are stored in the $\mathbf{S}_x$ matrix.

4.2.1.2 Prior information on the aerosol optical thickness

The prior information on the magnitude of AOT is set to very low value with a large corresponding uncertainty.

4.2.1.3 Prior information on the surface parameter spectral variability

Prior information concerning the spectral dependency of the surface anisotropy could also be used. The spectral variations of the surface anisotropy k, Θ and h are expected to be subject to some spectral dependencies. In the MISR aerosol algorithm for instance, this correlation is expressed as a spectral invariance of the normalized shape of the BRF (Diner et al. 2005). Spectral similarities in the surface reflectance are used to determine the correlation $r_{\tilde{\lambda}_i,\tilde{\lambda}_j}(x_s, \Omega)$ of each parameter x_s between bands $\tilde{\lambda}_i$ and $\tilde{\lambda}_j$. The elements of $\mathbf{S}_x$ write

$$\mathbf{S}_x(i,j) = r_{\tilde{\lambda}_i,\tilde{\lambda}_j}(x, \Omega)\, \sigma_i\, \sigma_j. \quad (26)$$

This option is not activated for the processing of SEVIRI solar channels as the spectral distance between these bands is too large.

4.2.1.4 Prior information on AOT temporal variability

AOT is not expected to change rapidly on an hourly basis. Hence, the speed at which hourly AOT can change in time is constrained. In order to derive the equation of this error contribution, let us define the stochastic variable x as being the deviation between the state variable and its mean such that

$$x = X - \overline{X} \tag{27}$$

The variable x is assumed to be a white noise process, so that $E\{x\} = 0$ and $E\{x^2\} = \sigma_x^2$. Assuming that the daily aerosol load variations are represented by a first order auto regressive model, the equation that describes in time the evolution of x can be written

$$x_{t+1} = \alpha\, x_t + \beta \tag{28}$$

where α is the autocorrelation coefficient between time t and $t+1$, derived from AERONET data temporal analysis, and β is a white noise process.

If x_{t_i} is the value of the state variable at time t_i, it is possible to derive the value of x_{t_j} at time t_j by applying recursively Equation (28). It can be easily shown that an expression of an estimate of the difference between x_{t_j} and x_{t_i} can be written as

$$x_{t_j} - x_{t_i} = \left(\alpha^j - 1\right)\; x_{t_i} + \alpha^{j-1} \cdot \beta_1 + ... + \beta_j \tag{29}$$

The uncertainty associated to the assumption $x_{t_j} - x_{t_i} = 0$ is defined as

$$\sigma_A^2(t_{i,j}, \tilde{\lambda}) = \left(A_d + \frac{A_a}{1 + \exp(-A_b\,(|t_i - t_j| - A_c))} \right)^2 \tag{30}$$

The values of the coefficients A_a, A_b, A_c and A_d are given in Section (6.1). The elements of $\sigma_A^2(t_{i,j})$ are stored in the $\mathbf{S}_a$ matrix. The resulting model is shown in Figure 3.

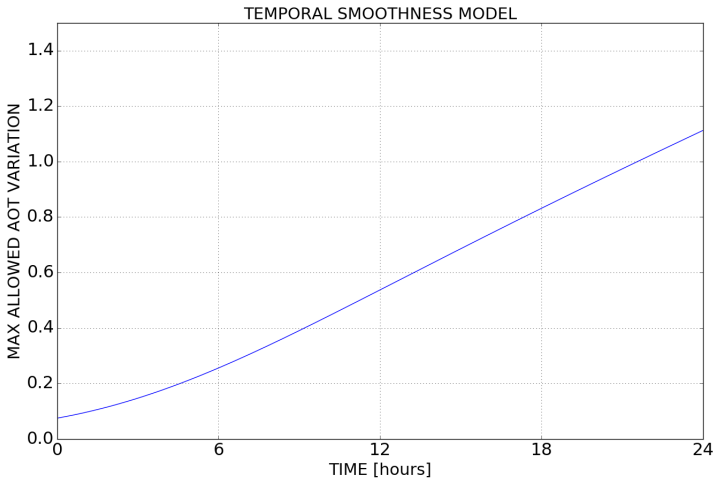

Figure 3: Temporal smoothness model.

4.2.1.5 Prior information on AOT spectral variability Similarly, constraints on the spectral variability of the AOT can be used as suggested by Dubovik et al. (2011). This dependency is used to determine the correlation of $\tau_a(\tilde{\lambda})$ between bands $\tilde{\lambda}_i$ and $\tilde{\lambda}_j$. Within a pre-defined aerosol class c, we have

$$\tau_c(\tilde{\lambda}_i) = \tau_c(\tilde{\lambda}_j)\ \frac{\sigma_e(\tilde{\lambda}_i)}{\sigma_e(\tilde{\lambda}_j)} \tag{31}$$

where σ_e is the extinction coefficient. As each optical thickness in each processed spectral band $\tilde{\lambda}$ for a given aerosol class is retrieved independently, the spectral variation of τ_c is constrained assuming that the retrieved optical thickness $\tau_c(\tilde{\lambda}_i)$ in band $\tilde{\lambda}_i$ could be related to the one in band $\tilde{\lambda}_j$ with Equation (31) assuming a constant error σ_L.

4.2.2 Measurement system uncertainty

A reliable estimation of the measurement system uncertainty is one of the most critical aspects of the CISAR algorithm as it strongly determines the likelihood of the solution. The measurement system total error covariance matrix $\mathbf{S}_y$ is composed of

$$\mathbf{S}_y = \mathbf{S}_N + \mathbf{S}_B + \mathbf{S}_F \tag{32}$$

with

S_N the radiometric noise matrix;

S_B the equivalent model parameter matrix;

S_F the forward model uncertainty matrix.

All uncertainties are expressed in BRF. The elements i, j of $\mathbf{S}_y$ are composed of

$$\mathbf{S}_y(i,j) = \begin{pmatrix} \sigma^2(\bar{t}_0,\tilde{\lambda}_1) & r_{12}\sigma(\bar{t}_0,\tilde{\lambda}_1)\sigma(\bar{t}_1,\tilde{\lambda}_1) & \cdots & r_{1N}\sigma(\bar{t}_0,\tilde{\lambda}_1)\sigma(\bar{t}_N,\tilde{\lambda}_1) & r_{1N+1}\sigma(\bar{t}_0,\tilde{\lambda}_1)\sigma(\bar{t}_1,\tilde{\lambda}_2) & \cdots & r_{1M_y}\sigma(\bar{t}_0,\tilde{\lambda}_1)\sigma(\bar{t}_N,\tilde{\lambda}_3) \\ r_{21}\sigma(\bar{t}_1,\tilde{\lambda}_1)\sigma(\bar{t}_0,\tilde{\lambda}_1) & \sigma^2(\bar{t}_1,\tilde{\lambda}_1) & \cdots & \cdots & \cdots & \cdots & r_{2M_y}\sigma(\bar{t}_1,\tilde{\lambda}_1)\sigma(\bar{t}_N,\tilde{\lambda}_3) \\ \vdots & \cdots & \ddots & \cdots & \cdots & \cdots & \vdots \\ r_{2M_y}\sigma(\bar{t}_0,\tilde{\lambda}_1)\sigma(\bar{t}_N,\tilde{\lambda}_3) & \cdots & \cdots & \cdots & \cdots & \ddots & \sigma^2(\bar{t}_N,\tilde{\lambda}_3) \end{pmatrix} \tag{33}$$

4.2.2.1 Radiometric uncertainty $\mathbf{S}_N$ The radiometric noise is composed of (*i*) the instrument noise due to the dark current; (*ii*) the difference between the detector gain; (*iii*) the number of digitalization level; and finally (*iv*) the geo-location/coregistration accuracy. As SEVIRI images are accumulated during the course of the day to form a virtual multi-angular observation, any inaccuracies in the rectification are converted into an equivalent radiometric uncertainty.

For an image acquired at time $\bar{t}$ in the band $\tilde{\lambda}$, the contribution of (*i*) and (*ii*) writes

$$\sigma_n^2(\bar{t},\tilde{\lambda},\mathbf{p}) = \left(\frac{\mathbf{y}(t,\tilde{\lambda},\mathbf{p})}{K(t,\tilde{\lambda},\mathbf{p})}\right)^2 \left(\frac{1}{n_d}\sum_{n_d}\sigma_d^2(\bar{t},\tilde{\lambda}) + \frac{1}{n_d-1}\sum_{n_d}\left(K_0(d\bar{t},\tilde{\lambda}) - \bar{K}_0(\bar{t},\tilde{\lambda})\right)^2\right) \tag{34}$$

where n_d is the number of detectors, $\sigma_d^2(\bar{t}, \tilde{\lambda})$ is the standard deviation of K_0 for detector d of the channel $\tilde{\lambda}$ for the image acquire at time $\bar{t}$. The first term of the right hand side accounts for the noise of the individual detector (*i*) whereas the second terms accounts for the difference between the detectors (*ii*). This uncertainty is the same for all pixels of an image but differs from channel to channel and slot to slot.

The digitalization error (*iii*), despite very small on SEVIRI , is calculated to keep the compatibility with the processing of Meteosat First Generation (MFG) data. This error writes

$$\sigma_i^2(\tilde{\lambda}) = \left(\mathbf{y}(t, \tilde{\lambda}) \, \frac{2 \, K(t, \tilde{\lambda})}{2^b} \right)^2 \tag{35}$$

where b is the number of digitalization bits. The geo-location/coregistration inaccuracies σ_r (*iv*) need to be estimated for each pixel of an image

$$\sigma_r^2(t, \tilde{\lambda}, \mathbf{p}) = \left(\frac{\partial \mathbf{y}(t, \tilde{\lambda}, p_x, p_y)}{\partial p_x} \sigma_x(\bar{t}, \tilde{\lambda}) \right)^2 + \left(\frac{\partial \mathbf{y}(t, \tilde{\lambda}, p_x, p_y)}{\partial p_y} \sigma_y(\bar{t}, \tilde{\lambda}) \right)^2 \tag{36}$$

where $\sigma_{x,y}$ is the geo-location/coregistration standard deviation of channel $\tilde{\lambda}$ acquired at time $\bar{t}$. It is expected that the rectification noise is spectrally correlated but not temporally correlated. Hence the terms of the matrix $\mathbf{S}_N$ writes

$$\mathbf{S}_N(i,j) = \delta(i,j)\sigma_n^2(\bar{t}, \tilde{\lambda}, \mathbf{p}) + \delta(i,j)\sigma_i^2(\tilde{\lambda}) + r_r(i,j)\sigma_r(i)\sigma_r(j) \tag{37}$$

where $\delta(i,j)$ is the Dirac function ($\delta(i,j) = 0$ when $i \neq j$). The rectification correlation r_r is 1 when i and j concern the same SEVIRI band and 0 otherwise.

TBD: Verify the need to account for the temporal and spectral correlation of the rectification noise.

4.2.2.2 Equivalent model parameter noise $\mathbf{S}_B$

This noise is due to the uncertainties on $\mathbf{b}(\bar{t})$. It is converted in Equivalent Model Parameter Noise (EQMPN). As this piece of information comes from two independent sources of information, they are supposed not correlated.

$$\sigma_B^2(\mathbf{b}; \tilde{\lambda}, \Omega_0, \Omega_v) = \left(\frac{\partial y(\mathbf{x}, U_{oz}; \Omega, \tilde{\lambda})}{\partial U_{oz}} \sigma_{U_{oz}} \right)^2 + \left(\frac{\partial y(\mathbf{x}, U_{wv}; \Omega, \tilde{\lambda})}{\partial U_{wv}} \sigma_{U_{wv}} \right)^2 \tag{38}$$

The terms of the matrix $\mathbf{S}_B$ write

$$\mathbf{S}_B(i,j) = \delta(i,j) \, \sigma_B^2(\tilde{\lambda}, \Omega) \tag{39}$$

TBD: Verify the spectral correlation of the model uncertainty σ_B.

4.2.2.3 Forward model uncertainty $\mathbf{S}_F$ This noise results from fast forward model assumptions and approximations described in Section 3.1. Let $y_R(\mathbf{x}, \mathbf{b})$ be an accurate forward model with an explicit representation of the atmospheric vertical profile. A global estimation of this error is performed that does not depend on the actual value of $\mathbf{x}$. The error covariance is

$$\sigma_F^2(\tilde{\lambda}, \Omega_0, \Omega_v, \phi) = \Big(\mathbf{y}(\Omega, \tilde{\lambda})\Big)^2 \frac{1}{N} \sum_{\{\mathbf{x},\mathbf{b}\}} \left(\frac{y_m(\mathbf{x}_\Delta, \mathbf{b}_\Delta, \Omega_\Delta) - y_R(\mathbf{x}, \mathbf{b}, \Omega)}{y_R(\mathbf{x}, \mathbf{b}, \Omega)} \right)^2 \tag{40}$$

where $\mathbf{x}_\Delta$ represents the discretized value of $\mathbf{x}$ and $\{\mathbf{x}, \mathbf{b}\}$ is the domain of variation of $\mathbf{x}$ and $\mathbf{b}$. The terms of the matrix $\mathbf{S}_F$ writes

$$\mathbf{S}_F(i, j) = \sigma_F^2(\tilde{\lambda}, \Omega_0, \Omega_v, \phi) \tag{41}$$

TBD: Verify if $\mathbf{S}_F$ is a diagonal matrix.

4.3 Angular and spectral inversion

4.3.1 Cloud filtering

The cloud mask generated by the Nowcasting SAF (Meteo France 2013). The cloud mask (CMa), developed within the SAF Nowcasting context, aims to support nowcasting applications, and additionally the remote-sensing of continental and oceanic surfaces. The CMa allows identifying cloud free areas where other products (total or layer precipitable water, land or sea surface temperatures, snow/ice cover delineation) may be computed. It also allows identifying cloudy areas where other products (cloud types and cloud top temperature/height) may be derived. This mask is used to remove cloudy or partially cloudy pixels in the the accumulated series of SEVIRI observations.

In order to reduce the computer time dedicated to the inversion, only one clear-sky SEVIRI observations per hour is kept. If more than one clear-sky observation is available during a one hour interval, only the one with the smallest radiometric uncertainty is kept. However, if there is less than N_c clear-sky observations during one day, all the observations of that day are kept.

TBD: Verify the benefit of exploiting the results of the individual tests applied in the CMa product not to remove dust storm and fire smoke cases.

The size of the measurement vector after cloud screening and data reduction is noted n_y. The inversion process takes place only when the number of clear-sky observations within the accumulation period is larger than $4 + N_a$ where N_a is the number of inverted aerosol classes.

4.3.2 Definition of the cost function J

The fundamental principle of optimal estimation is to maximise the probability of the retrieved state conditional on the value of the measurements and any prior information. Formally, it is required to maximise the conditional probability $P = P(\mathbf{x}|\mathbf{y}_{\Omega\tilde{\Lambda}}, \mathbf{x}_\mathbf{b}, \mathbf{b})$ with respect to the values of the state vector $\mathbf{x}$ (Section 3.7), where $\mathbf{x}_\mathbf{b}$ is the prior value of the state vector (Section 4.2.1) and $\mathbf{b}$ are

all the other elements of the radiative transfer, called forward model parameters (Section 3.7). The assumption is made that uncertainties in the measurements ($\mathbf{S}_y$ Equation 32), and prior ($\mathbf{S}_x$ Equation 26) are normally distributed with zero mean. Then, the conditional probability takes on the quadratic form:

$$\begin{aligned} P(\mathbf{x}) \quad \propto \quad & \exp\left[-\left(y(\mathbf{x},\mathbf{b},\Omega)-\mathbf{y}_{\Omega\tilde{\Lambda}}\right)^T \mathbf{S}_y^{-1}\left(y(\mathbf{x},\mathbf{b},\Omega)-\mathbf{y}_{\Omega\tilde{\Lambda}}\right)\right] \\ & \exp\left[-\left(\mathbf{x}-\mathbf{x}_b\right)^T \mathbf{S}_x^{-1}\left(\mathbf{x}-\mathbf{x}_b\right)\right] \\ & \exp\left[-\mathbf{x}^T\,\mathbf{H}_a^T\,\mathbf{S}_a^{-1}\,\mathbf{H}_a\,\mathbf{x}\right] \\ & \exp\left[-\mathbf{x}^T\,\mathbf{H}_l^T\,\mathbf{S}_l^{-1}\,\mathbf{H}_l\,\mathbf{x}\right] \end{aligned} \tag{42}$$

where the first two terms represent weighted deviations from measurements and the prior state parameters respectively, the third the AOT temporal smoothness constraints and the fourth the AOT spectral constraints.

The two matrices $\mathbf{H}_a$ and $\mathbf{H}_l$ can be written as block diagonal matrices

$$\mathbf{H} = \begin{pmatrix} \mathbf{H}^{\rho_0} & \mathbf{0} & \mathbf{0} & \mathbf{0} & \mathbf{0} \\ \mathbf{0} & \mathbf{H}^{k} & \mathbf{0} & \mathbf{0} & \mathbf{0} \\ \mathbf{0} & \mathbf{0} & \mathbf{H}^{\theta} & \mathbf{0} & \mathbf{0} \\ \mathbf{0} & \mathbf{0} & \mathbf{0} & \mathbf{H}^{\rho_c} & \mathbf{0} \\ \mathbf{0} & \mathbf{0} & \mathbf{0} & \mathbf{0} & \mathbf{H}^{\tau} \end{pmatrix} \tag{43}$$

where the four blocks $\mathbf{H}^{\rho_0}$, $\mathbf{H}^{k}$, $\mathbf{H}^{\theta}$ and $\mathbf{H}^{\rho_c}$ are zero blocks.

The submatrix $\mathbf{H}_a^{\tau}$ can also be written using diagonal blocks $\mathbf{H}^{\tau}_{a;\tilde{\lambda},c}$. For a given spectral band $\tilde{\lambda}$ and aerosol class c, the block $\mathbf{H}^{\tau}_{a;\tilde{\lambda},c}$ is defined as follows

$$\mathbf{H}^{\tau}_{a;\tilde{\lambda},c}\,\boldsymbol{\tau}_{\tilde{\lambda},c} = \begin{pmatrix} 1 & -1 & 0 & \dots & \dots \\ 0 & 1 & -1 & 0 & \dots \\ \dots & \dots & \dots & \dots & \dots \\ \dots & \dots & \dots & 1 & -1 \\ \dots & \dots & \dots & \dots & 0 \end{pmatrix} \begin{pmatrix} \tau_{\tilde{\lambda},c,1} \\ \tau_{\tilde{\lambda},c,2} \\ \vdots \\ \tau_{\tilde{\lambda},c,N_t-1} \\ \tau_{\tilde{\lambda},c,1,N_t} \end{pmatrix} \tag{44}$$

In the same way, the submatrix $\mathbf{H}_l^{\tau}$ can be written using diagonal blocks $\mathbf{H}^{\tau}_{l;c,t}$. For a given aerosol class c and time t, the block $\mathbf{H}^{\tau}_{l;c,t}$ is defined as follows

$$\mathbf{H}^{\tau}_{l;c,t}\,\boldsymbol{\tau}_{c,t} = \begin{pmatrix} 0 & 0 & 0 & \dots & 0 \\ -\frac{\epsilon_2}{\epsilon_1} & 1 & 0 & \dots & 0 \\ 0 & -\frac{\epsilon_3}{\epsilon_2} & 1 & \dots & 0 \\ \dots & \dots & \dots & \ddots & 0 \\ \dots & \dots & \dots & -\frac{\epsilon_{N_\lambda}}{\epsilon_{N_\lambda-1}} & 1 \end{pmatrix} \begin{pmatrix} \tau_{1,c,t} \\ \tau_{2,c,t} \\ \tau_{3,c,t} \\ \vdots \\ \tau_{N_{\tilde{\lambda}},c,t} \end{pmatrix} \tag{45}$$

Maximising probability is equivalent to minimising the negative logarithm, so that we equivalently minimise J where

$$J(\mathbf{x}) = J_y(\mathbf{x}) + J_x(\mathbf{x}) + J_a(\mathbf{x}) + J_l(\mathbf{x}) \tag{46}$$

with

$$J_y(\mathbf{x}) = \left(y_m(\mathbf{x},\mathbf{b},\Omega) - \mathbf{y}_{\Omega\tilde{\Lambda}}\right) \mathbf{S}_y^{-1} \left(y_m(\mathbf{x},\mathbf{b},\Omega) - \mathbf{y}_{\Omega\tilde{\Lambda}}\right)^T \quad (47)$$

$$J_x(\mathbf{x}) = \left(\mathbf{x} - \mathbf{x}_b\right) \mathbf{S}_x^{-1} \left(\mathbf{x} - \mathbf{x}_b\right)^T \quad (48)$$

$$J_a(\mathbf{x}) = \mathbf{x}^T \mathbf{H}_a^T \mathbf{S}_a^{-1} \mathbf{H}_a \mathbf{x} \quad (49)$$

$$J_l(\mathbf{x}) = \mathbf{x}^T \mathbf{H}_l^T \mathbf{S}_l^{-1} \mathbf{H}_l \mathbf{x} \quad (50)$$

Notice that J is minimized with respect to the state variable $\mathbf{x}$, so that the derivative of J is independent of the model parameters $\mathbf{b}$ which therefore cannot be part of the solution. The first term of the right hand side of Equation (46) expresses the contribution due to the observation and is noted J_y whereas the second term represents the cost due to the prior information and is noted J_x so that $J = J_y + J_x$. The need for angular sampling to document the surface anisotropy leads to an unbalanced size of n_x and n_y with $n_y > n_x$. According to Dubovik et al. (2006), these additional observations should improve the retrieval as, from a statistical point of view, performing straightforward repetition of the the same observation with established unchanged accuracy implies that the variance of the observation should decrease. Accordingly, the elements of the covariance matrix should decrease. Thus, from a theoretical point of view, repeating similar observations results in some enhancements of retrieval accuracy which should be proportional to the ratio n_y/n_x. Hence, the cost function which is actually minimized is $J = J_y + n_y/n_x\ (J_x + J_a + J_l)$.

4.3.2.1 Minimization of J This section addresses the problem of the minimization of J, *i.e.*, finding the solution $\hat{\mathbf{x}}$. This is an area where many techniques and methods can be employed and where tuning of the adopted scheme can turn out to be as important as the scheme itself. Essentially any method of finding the minimum is acceptable in a sense, with the caveat that in an operational context it must be robust and fast. The particular characteristics of this problem are that:

- **First and second derivatives of J (with respect to $\mathbf{x}$) are available and continuous** , which implies descent algorithms that make use of the local gradient are possible and these are generally faster than methods that do not.
- **Multiple minima are unlikely** This condition is however not met in the present case, and the solution is searched for different first guess values (see Section 4.3.2.2)
- **J is likely to be approximately quadratic in the region of the solution, far from quadratic elsewhere.** This characteristics is a result of the reasonably strongly non-linear nature of the forward (radiative transfer) problem. It means that quick convergence from a poor starting position is unlikely.

The cost function $J(\hat{\mathbf{x}})$ is minimized, for example using a steepest descent method, or the Levenberg-Marquardt method (combined steepest-descent method / Gauss-Newton method, as described in Section (4.3.2.3)). This minimization is performed individually for each defined aerosol class.

The first and second derivatives of J with respect to $\mathbf{x}$ are given by:

$$\mathbf{J}' = \frac{\partial J}{\partial \mathbf{x}} = \mathbf{K}_x^T \mathbf{S}_y^{-1} (y_m(\mathbf{x},\mathbf{b},\Omega) - \mathbf{y}_{\Omega\tilde{\Lambda}}) + \mathbf{S}_x^{-1}\ (\mathbf{x} - \mathbf{x}_b) + \mathbf{H}_a^T\ \mathbf{S}_a^{-1}\ \mathbf{H}_a\ \mathbf{x} + \mathbf{H}_l^T\ \mathbf{S}_l^{-1}\ \mathbf{H}_l\ \mathbf{x} \quad (51)$$

$$\mathbf{J}'' = \frac{\partial^2 J}{\partial \mathbf{x}^2} = \mathbf{K}_x^T \, \mathbf{S}_y^{-1} \, \mathbf{K}_x + \mathbf{S}_x^{-1} + \mathbf{H}_a^T \, \mathbf{S}_a^{-1} \, \mathbf{H}_a + \mathbf{H}_l^T \, \mathbf{S}_l^{-1} \, \mathbf{H}_l \tag{52}$$

The expression for $\mathbf{J}''$ is a commonly used approximation in that $\mathbf{K}_x$ is assumed to be independent of $\mathbf{x}$, *i.e.*, the radiative transfer is linear in $\mathbf{x}$. The estimation of the Jacobian matrix $\mathbf{K}_x$ is described in Section (3.6). This is only strictly true near the solution (in the region where J is quadratic) but (see next section) since $\mathbf{J}''$ is only employed near the solution the approximation is acceptable.

4.3.2.2 First guess As the problem to be solved is not linear, the presence of local minima is very likely to happen. Hence, when a minimum value is found, an exploration should be made around a minimum in order to determine whether or not it is a local minimum. Such exploration phase could be computationally expensive. This is particularly true when solving a coupled surface-atmosphere system where the magnitude of the surface reflectance is competing with aerosol scattering. It is therefore necessary to carefully select the first guess value $\mathbf{x_0}$ in order to minimize the chance to end in a local minimum.

As the surface parameters $\mathbf{x_s}$ are assumed constant during the accumulation period, only one set of first guess value has to be provided. This value is derived from the prior information $\mathbf{x_b}$

$$\mathbf{x_0}(t_d) = \mathbf{x_b}(t_d) + -1^{t_d} \, \alpha_0 \, \sigma_{\mathbf{x_b}}(t_d) \tag{53}$$

where t_d is the index of the processed period and α_0 a perturbation factor.

For the hourly AOT parameter, the first guess values of are set alternatively to a low value τ_{low} and a large one τ_{high}.

4.3.2.3 Marquardt descent algorithm To find the minimum a "first guess" state vector $\mathbf{x}_0$ is selected as described in Section 4.3.2.2 and proceed to make steps, $\delta\mathbf{x}_n$, adjusting the length of the steps according to the distance from the minimum, *i.e.*the lenght of steps decreases when approaching the solution. Assuming the value of J decreases at each step then the updated $\mathbf{x}$ vector is taking the process towards the cost function minimum. The CISAR algorithm relies on the Levenberg-Marquardt method to compute the descent. The use of this algorithm is consistent with the three points made above. The rationale of the Levenberg-Marquardt algorithm is to use a weighted combination of steepest descent and Gauss-Newton descent according to the characteristics of the cost function. Thus, when the cost function is near quadratic (generally near the solution) the efficiency of the Gauss-Newton algorithm is employed and when the cost function is far from quadratic (generally when far from the solution) the robustness of the Steepest Descent algorithm is favoured.

The Steepest Descent algorithm is intuitively the simplest. The vector $-\mathbf{J}'$ defines the "downward" direction of the local steepest gradient. A move $\delta\mathbf{x} = -\mathbf{J}'$ is almost certainly at least approximately in the direction of the minimum although it may be too far or barely far enough. The step is therefore usually scaled, $\delta\mathbf{x} = -\alpha\mathbf{J}'$ where α is variable. If J is found to be decreasing α can be increased to move faster; if J increases then α is reduced until J decreases. J must eventually decrease with this method otherwise something is wrong with the calculation of $\partial J/\partial\mathbf{x}$. The problem with steepest descent is that it can be very slow to converge, especially near the solution where the gradient necessarily becomes small. It is however, very robust.

The Gauss–Newton method is a modification of Newton's method which is very fast near the solution. The Gauss–Newton method compared to the Newton's method has the advantage that the second derivative of J, which can be challenging to compute, is not required.

The second derivative $\mathbf{J}''$ is calculated only once, after the process of the Levenberg-Marquardt algorithm, to compute the output uncertainties.

The Levenberg-Marquardt inversion algorithm starts with an initialisation to set the cost at the first guess state (see Section 4.3.2.2), $J(\mathbf{x}_0)$, and, normally, to set the initial state for the iteration equal to the first guess, $\mathbf{x}_n = \mathbf{x}_0$.

A maximum number of iterations is permitted, and if no convergence is reached after this number, the algorithm exits at the current state (the iteration count is part of the standard output of the CISAR so that this exit condition can be checked in the results).

4.3.2.4 Convergence criteria The iteration process is stopped when the decrease in J between iterations, δJ_n is so small as to be negligible or when the number of iterations reaches a maximum threshold defined at the begining of the inversion.

4.3.3 Quality control

TBD: Finalize the quality control.

4.3.4 Linear error analysis

The retrieval uncertainty is based on the OE theory, assuming a linear behaviour of $y(\mathbf{x}, \mathbf{b})$ in the vicinity of the solution $\hat{\mathbf{x}}$. Under this condition, the retrieval uncertainty $\sigma_{\hat{\mathbf{x}}}$ is determined by the shape of $J(\mathbf{x})$ in $\hat{\mathbf{x}}$

$$\sigma^2_{\hat{\mathbf{x}}} = \left(\frac{\partial^2 J(\mathbf{x})}{\partial \mathbf{x}^2} \right)^{-1} = \left(\mathbf{K}_x^T \, \mathbf{S}_y^{-1} \, \mathbf{K}_x + \mathbf{S}_x^{-1} + \hat{\mathbf{S}}_a + \hat{\mathbf{S}}_l \right)^{-1} \tag{54}$$

where $\mathbf{K}_x$ is the gradient of $y(\mathbf{x}, \mathbf{b})$ calculated in $\hat{\mathbf{x}}$. The uncertainty $\sigma^2_{\hat{\mathbf{x}}}$ is actually composed of two distinct contributions:

- **Null space uncertainty** This uncertainty is given by

  $$\mathbf{S}_N = (\mathbf{D}_y \mathbf{K}_x - \mathbf{m}) \, \mathbf{S}_s \, (\mathbf{D}_y \mathbf{K}_x - \mathbf{m}) \tag{55}$$

  where $\mathbf{D}_y$ is the inverse operator $\mathbf{D}_y = \partial \hat{\mathbf{x}} / \partial y_m$

  $$\mathbf{D}_y = \left(\mathbf{K}_x^T \, \mathbf{S}_y^{-1} \, \mathbf{K}_x + \mathbf{S}_x^{-1} + \hat{\mathbf{S}}_a + \hat{\mathbf{S}}_l \right)^{-1} \mathbf{K}_x^T \, \mathbf{S}_y^{-1} \tag{56}$$

  $\mathbf{S}_N$ expresses the uncertainty that arises from a basic lack of information in the measurement system.

- **Measurement uncertainty** This uncertainty is given by

  $$\mathbf{S}_M = \mathbf{D}_y \, \mathbf{S}_y \, \mathbf{D}_y^T \tag{57}$$

  The model parameter uncertainty is included into the measurement uncertainty.

4.4 Product generation

At the end of the inversion procedure, a product is generated. One product, ie, NetCDF file, is generated for each hourly retrieved aerosol optical thickness. These product data files are named according to the following convention

`YYYYMMDDHH-ESACCI-L2P_AEROSOL-AER_PRODUCTS-SEVIRI -MSG-CISAR-fvXX.XX.nc`

where

`YYYY`	is the year of the current retrieval
`MM`	is the month of the current retrieval
`DD`	is the day of the current retrieval
`HH`	is the hour of the current retrieval
`XX.XX`	us the version of the algorithm

5 ASSUMPTIONS AND LIMITATIONS

5.1 Assumptions

The CISAR algorithm relies on the following assumptions:

1. Satellite observations are unbiased with an uncertainty characterised by a Gaussian distribution.
2. The radiation regime at the spatial scale of a SEVIRI pixel can be represented with a one dimensional horizontally homogeneous RTM.
3. Topography and slope effects are ignored, *i.e.*, pixels are assumed flat.
4. A limited number of aerosol classes can be used to describe the spectral variability of their properties.
5. The surface radiative properties do not change during the course of the accumulation period.
6. The RPV model is considered adequate to accurately represent all types of surface BRF everywhere and all year long at the spatial scale of a SEVIRI pixel.

5.2 Limitations

The following limitations apply to the CISAR algorithm:

1. SEVIRI observations are processed only of the corresponding Sun and observation zenith angles are less than 70°.
2. No retrieval will take place if the number of SEVIRI observations per channel is smaller than $4 + N_a + 1$ where N_a is the number of aerosol classes.

6 Input data requirements

6.1 Setup parameters

The following main run-time setup parameters are used within CISAR :

Symbol	**Description**	Default value
	Maximum number of iterations	20
$\theta_{\max}$	Maximum processed sun and viewing zenith angles	70°
N_c	Threshold value for the minimum number of daily clear-sky observations. No hourly data reduction takes place below this value.	6
A_a	Coefficient of Equation (30)	1.05
A_b	Coefficient of Equation (30)	0.20
A_c	Coefficient of Equation (30)	2.00
A_d	Coefficient of Equation (30)	0.075
N_d	Duration in day of the accumulation period	5
σ_L	Uncertainty on AOT spectral relationship defined in Section (4.2.1.5)	0.02
$\sigma_{\min}$	Minimum error on the surface parameters	0.02
τ_{low}	Minimum AOT first guess value	0.01
τ_{high}	Maximum AOT first guess value	1.00

6.2 SEVIRI radiances

On top of digital count values, acquisition time and the following information from the level 1.5 file header are needed:

Field	Variable	**DESCRIPTION**
	$K_0(\tilde{\lambda}, d)$	Detector d offset of band $\tilde{\lambda}$
	$\tilde{K_0}(\tilde{\lambda})$	Mean offset of band $\tilde{\lambda}$
	$\sigma_d(\tilde{\lambda})$	Standard deviation of $\tilde{K_0}(\tilde{\lambda})$
	$\sigma_x(\tilde{\lambda})$	E-W rectification uncertainty of band $\tilde{\lambda}$
	$\sigma_y(\tilde{\lambda})$	N-S rectification uncertainty of band $\tilde{\lambda}$
	$n_d(\tilde{\lambda})$	number of detector of band $\tilde{\lambda}$
	$E_0(\tilde{\lambda})$	Irradiance within band $\tilde{\lambda}$ at 1 AU

6.3 Ancillary information

The following ancillary information is requested:

Data	Type	Unit	Description
CMa	Dynamic	N/A	Nowcasting SAF cloud mask. This mask is provided at SEVIRI native temporal and spatial resolution
TCWV	Dynamic	kg/m^2	Total column water vapour taken from ECMWF reanalysis data, linearly interpolated in time, bilinearly in space
TCO3	Dynamic	Dobson	Total column ozone taken from ECMWF reanalysis data, linearly interpolated in time, bilinearly in space
SRFP	Dynamic	hPa	Surface pressure taken from ECMWF reanalysis data. Surface pressure is calculated from a standard value of 1013.25 hPa at sea level and is converted to pressure at a certain height, using a conversion formula of Plummer et al. (2003).
SWS	Dynamic	m/s	Surface wind speed taken from ECMWF reanalysis data
LSM	Static	N/A	Land-sea mask
LAT	Static	degree	Pixel latitude
LON	Static	degree	Pixel longitude

Dynamic data are updated for each processed L1b image. Static data are computed once and for all.

6.4 Product data output format

At the end of the inversion procedure, a product is generated. One product, ie, NetCDF file, is generated for each hourly retrieved aerosol optical thickness. These product data files are named according to the following convention

`YYYYMMDDHH-ESACCI-L2P_AEROSOL-AER_PRODUCTS-SEVIRI -MSG-CISAR-fvXX.XX.nc`

where

`YYYY` is the year of the current retrieval
`MM` is the month of the current retrieval
`DD` is the day of the current retrieval
`HH` is the hour of the current retrieval
`XX.XX` us the version of the algorithm

An hourly AOT product data contains the following fields:

Name	Symbol	Eq.	Description
AOD550	$\hat{\tau}_a(0.55)$		Total aerosol optical thickness in layer L_a interpolated at 0.55μm
AOD670	$\hat{\tau}_a(0.67)$		Total aerosol optical thickness in layer L_a in SEVIRI band VIS0.6
AOD870	$\hat{\tau}_a(0.87)$		Total aerosol optical thickness in layer L_a in SEVIRI band VIS0.8
AOD1600	$\hat{\tau}_a(1.6)$		Total aerosol optical thickness in layer L_a in SEVIRI band NIR1.6
FM_AOD550	$\hat{\tau}_a(0.55)$		Fraction of AOD ascribed to fine mode aerosols particles at 0.55μm
FM_AOD670	$\hat{\tau}_a(0.67)$		Fraction of AOD ascribed to fine mode aerosols particles in SEVIRI band VIS0.6
FM_AOD870	$\hat{\tau}_a(0.87)$		Fraction of AOD ascribed to fine mode aerosols particles in SEVIRI band VIS0.8
FM_AOD1600	$\hat{\tau}_a(1.6)$		Fraction of AOD ascribed to fine mode aerosols particles in SEVIRI band NIR1.6
AOD550_uncertainty	$\sigma_{\hat{\tau}_a}(0.55)$	54	Estimated aerosol optical thickness uncertainty in layer L_a interpolated at 0.55μm
AOD670_uncertainty	$\sigma_{\hat{\tau}_a}(0.67)$	54	Estimated aerosol optical thickness uncertainty in layer L_a in SEVIRI band VIS0.6
AOD870_uncertainty	$\sigma_{\hat{\tau}_a}(0.87)$	54	Estimated aerosol optical thickness uncertainty in layer L_a in SEVIRI band VIS0.8
AOD1600_uncertainty	$\sigma_{\hat{\tau}_a}(1.6)$	54	Estimated aerosol optical thickness uncertainty in layer L_a in SEVIRI band NIR1.6
quality_flag			To be Defined
time			Actual acquisition time
LATITUDE			Pixel latitude in degree
LONGITUDE			Pixel longitude in degree

7 ALGORITHM IMPLEMENTATION

This section contains some practical information concerning the implementation of the CISAR algorithm. The systematic processing of SEVIRI data is performed using the GEneric DAta Processing Chain (GEDAP) algorithm, whose data flow is described in Section 7.2. GEDAP manages all the I/O for the retrieval algorithms. For this purpose, satellites orbits or images are fisrt decomposed in Tiles if not already available. A *tile* is defined by a geographical coverage, spatial resolution and geographical projection.

7.1 Input data preparation

For the systematic processing of SEVIRI data, images are segmented into tiles composed of 100x100 pixels as shown in Figure (4).

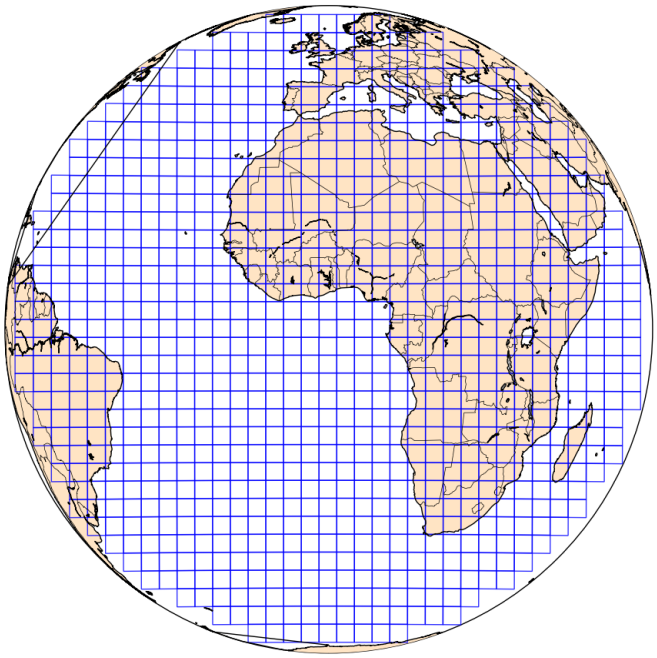

Figure 4: Segmentation of SEVIRI images into tiles.

GEDAP is using netCDF format to manage all the data. Prior to any other operation, one netCDF file, called Static Tile, is generated for each Tile, containing immutable data such as latitude, longitute, land/sea mask, elevation and aerosol layer height. SEVIRI data are accumulated during the accumulation and stored in Input Tiles, generated every 15 minutes. The Input Tiles also host the model parameters and the cloud mask.

7.2 Overall GEDAP data flow

The overall GEDAP data flow is presented in Figure (5). The processing is composed of three major steps:

1. **INPUT DATA PREPARATION** In this module, SEVIRI images are segmented in Tiles as shown on Figure (4). Count values are converted in TOA BRF and accumulated during N_d days together with all the ancillary information listed in Section (6.3). It also loads the prior information which is set to climatological background values when the first accumulation period is processed.

2. **INVERSION** At the end of the input data preparation, the inversion process takes place for each Tile. The solutions and associated uncertainties are stored in disk files. The prior information on the state of the surface is updated.

3. **PRODUCT GENERATION** When all the Tiles of a given accumulation period are processed, all the Tiles are combined to generate a single full-disk product. One NetCDF file described in Section (4.4) is generated per hourly AOT product.

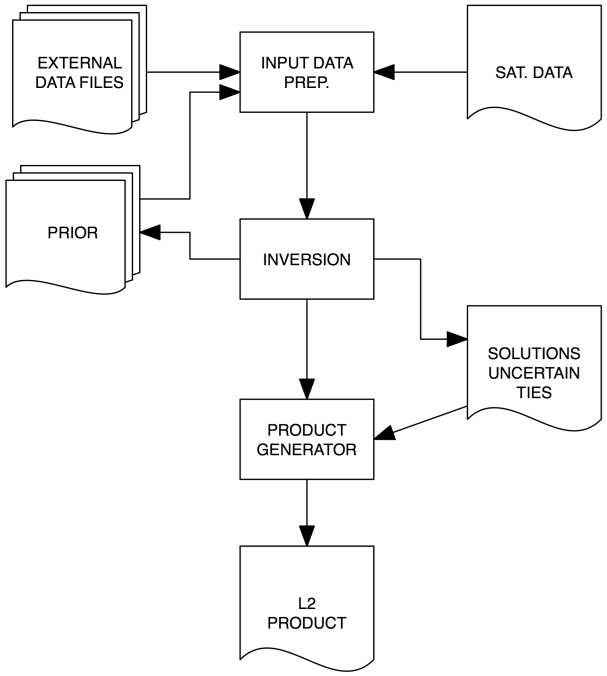

Figure 5: Overall data flow for the processing of SEVIRI data. The external data files are the files containing the ancillary information necessary to prepare the input files, together with the satellite data. When all the input files are prepared the inversion takes place. At the end of the inversion the prior is updated and the solution uncertainty estimated. The solutions and the relative uncertainties are finally combined to generate a single product.

References

Aminou, D. M. A., B. Jacquet, and F. Pasternak (1997). Characteristics of the meteosat second generation (msg) radiometer/imager: Seviri. In Europto (Ed.), *The European Symposium on Aerospace Remote Sensing*, Volume 3221, London, United Kingdom, pp. 19–31.

Cox, C. and W. Munk (1954, November). Measurement of the Roughness of the Sea Surface from Photographs of the Sun's Glitter. *Journal of the Optical Society of America 44*(11), 838–850.

Diner, D. J., J. V. Martonchik, R. A. Kahn, B. Pinty, N. Gobron, D. L. Nelson, and B. N. Holben (2005). Using angular and spectral shape similarity constraints to improve {MISR} aerosol and surface retrievals over land. *Remote Sensing of Environment 94*, 155–171.

Dubovik, O., M. Herman, A. Holdak, T. Lapyonok, D. Tanré, J. L. Deuzé, F. Ducos, A. Sinyuk, and A. Lopatin (2011). Statistically optimized inversion algorithm for enhanced retrieval of aerosol properties from spectral multi-angle polarimetric satellite observations. *Atmospheric Measurement Techniques 4*, 975–1018.

Dubovik, O., A. Sinyuk, T. Lapyonok, B. N. Holben, M. Mishchenko, P. Yang, T. F. Eck, H. Volten, O. Munoz, B. Veihelmann, W. J. van der Zande, J. F. Leon, M. Sorokin, and I. Slutsker (2006). Application of spheroid models to account for aerosol particle nonsphericity in remote sensing of desert dust. *Journal of Geophysical Research-Atmospheres 111*(D11), 11208–11208.

Engelsen, O., B. Pinty, M. M. Verstraete, and J. V. Martonchik (1996). Parametric bidirectional reflectance factor models: evaluation, improvements and applications.

Fischer, J. and H. Grassl (1984). Radiative transfer in an atmosphere-ocean system: an azimuthally dependent matrix-operator approach. *Applied Optics 23*, 1032–1039.

Govaerts, Y. (2004). Operation vicarious calibration of the solar channels of the {E}uropean meteorological geostationary satellites and its impact on geophysical product extraction. In M. Rast (Ed.), *Workshop on Inter-Comparison of Large Scale Optical and Infrared Sensors*, Noordwijk, The Netherlands, pp. 18–20. ESA.

Govaerts, Y. M., M. Clerici, and N. Clerbaux (2004). Operational calibration of the meteosat radiometer vis band. *IEEE Transactions on Geoscience and Remote Sensing 42*(9), 1900–1914.

Govaerts, Y. M., S. Wagner, A. Lattanzio, and P. Watts (2010, January). Joint retrieval of surface reflectance and aerosol optical depth from MSG/SEVIRI observations with an optimal estimation approach: 1. Theory. *Journal of Geophysical Research 115*(D02203), doi:10.1029/2009JD011779.

Koepke, P. (1984, June). Effective reflectance of oceanic whitecaps. *Applied Optics 23*(11), 1816.

Liu, Q. and E. Ruprecht (1996). Radiative transfer model: matrix operator method. *Applied Optics 35*, 4229–4237.

Meteo France (2013). Algorithm Theoretical Basis Document for "Cloud Products" (CMa-PGE01 v3.2, CT-PGE02 v2.2 & CTTH-PGE03 v2.2). Technical Report CTTH-PGE03 v2.2.

Moré, J. J., B. S. Garbow, and K. E. Hillstrom (1980). User Guide for MINPACK-1. *ANL-80-74, Argonne National Laboratory*.

Morel, A. (1988, September). Optical modeling of the upper ocean in relation to its biogenous matter content (case I waters). *Journal of Geophysical Research: Oceans 93*(C9), 10749–10768.

National Aeronautics and space Administration (1976). U.s. standard atmosphere.

Plummer, S., J. Chen, G. Dedieu, and M. Simon (2003). GLOBCARBON Detailed Processing Model. Technical Report GLBC-ESL-DPM-V1.3.

Rahman, H., B. Pinty, and M. M. Verstraete (1993). Coupled surface-atmosphere reflectance (CSAR) model. 2. Semiempirical surface model usable with NOAA Advanced Very High Resolution Radiometer Data. *Journal of Geophysical Research 98*(D11), 20,791–20,801.

Vermote, E. F., D. Tanre, J. L. Deuze, M. Herman, and J. J. Morcrette (1997). Second simulation of the satellite signal in the solar spectrum, 6s: An overview. *IEEE TGARS 35*(3), 675–686.

Wiscombe, W. J. (1977). The Delta-M Method: Rapid Yet Accurate Radiative Flux Calculations for Strongly Asymmetric Phase Functions. *Journal of Atmospheric Sciences 34*, 1408–1422.